the same in all phases. If the twist angles were greater, significantly further downfield shifted values would be expected, up to 373.5 ppm for $\tau = 90°$ (*12*). If electron donors such as solvent, anion, or the nearby Me groups closely approached the Si center, less downfield-shifted values would be expected. Similar shifts have been observed in related tin chemistry where the downfield ^{119}Sn chemical shift of the Bu_3Sn^+ cation is attenuated by axial interactions from Me groups of the counterion (*21*).

Additionally, the full ^{29}Si chemical shielding tensor can be determined in the solid state. The best fit to the slow magic-angle spinning spectrum (Fig. 4) gives 226.7 ppm for the isotropic shift, 185.5 ppm for the anisotropy (δ), and 0 for the asymmetry parameter (η). An axially symmetric tensor ($\eta = 0$) is required in the presence of a threefold rotational axis. On the basis of molecular symmetry, the equivalent δ_{xx} and δ_{yy} tensor components (319.5 ppm) lie within the coordination plane, whereas the δ_{zz} component (41.2 ppm) is aligned with the local C_3 axis. This distinctively large anisotropy under axial symmetry provides complementary structural characterization for the planar sp^2-hybridized silylium center. Related large anisotropies are seen in disilenes (*22*).

These results bring the differences between carbon and silicon into sharp focus (*3*). Because of its small size and intermediate value of electronegativity, carbon readily sustains coordinative unsaturation. Positive charge is readily stabilized by π conjugative (and hyperconjugative) effects. Silicon and the remainder of the group 14 elements are significantly larger in size and considerably more electropositive, so unsaturation is less easily stabilized by conjugative effects. Charge is less easily delocalized, and longer bonds to substituents invite access by nucleophiles so higher coordination numbers prevail. Substituent bonds are more polar and thus more easily cleaved. These features have conspired over the years to create the "silylium ion problem" that now appears to be solved. The situation with germylium and stannylium ions is less resolved (*20*, *21*, *23*).

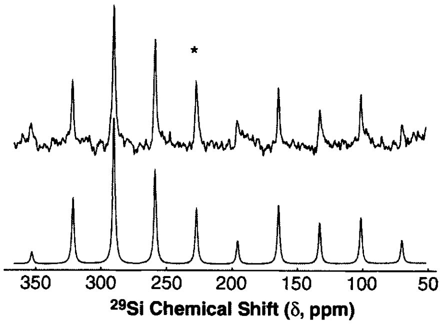

Fig. 4. The ^{1}H-decoupled ^{29}Si CPMAS (condensed phase magic angle spinning) NMR spectrum of $[Mes_3Si][H\text{-}CB_{11}Me_5Br_6]\cdot C_6H_6$ at a spinning rate of 2.5 kHz (top). The nonlinear least-squares fit of the sideband manifold (bottom) using the method of (*24*) gives an axially symmetric chemical shift tensor [$\sigma_{iso} = 226.7$ ppm (*); $\delta = 185.5$ ppm; $\eta = 0$].

References and Notes

1. For recent reviews on the silylium ion problem, see J. B. Lambert, L. Kania, S. Zhang [*Chem. Rev.* **95**, 1191 (1995)], as well as (*2–5*).
2. C. Maerker, J. Kapp, P. von R. Schleyer, in *Organosilicon Chemistry II*, N. Auner, J. Weis, Eds. (VCH, Weinheim, Germany, 1996), pp. 329–358.
3. C. A. Reed, *Acct. Chem. Res.* **31**, 325 (1998).
4. P. Lickiss, in *The Chemistry of Organic Silicon Compounds*, Z. Rappoport, Y. Apeloig, Eds. (Wiley, Chichester, UK, ed. 2, 1998), chap. 11.
5. J. B. Lambert, Y. Zhao, S. M. Zhang, *J. Phys. Org. Chem.* **14**, 370(2001).
6. G. A. Olah, *J. Org. Chem.* **66**, 5943 (2001).
7. C. A. Reed, Z. Xie, R. Bau, A. Benesi, *Science* **263**, 402 (1993).
8. J. B. Lambert, S. H. Zhang, C. L. Stern, J. C. Huffman, *Science* **260**, 1917 (1993).
9. C. A. Reed, K.-C. Kim, R. D. Bolskar, L. Mueller, *Science* **289**, 101 (2000).
10. J. B. Lambert, Y. Zhao, *Angew. Chem., Int. Ed. Engl.* **36**, 400 (1997).
11. J. B. Lambert, L. Lin, *J. Org. Chem.* **66**, 8537 (2001).
12. E. Kraka, C. P. Sosa , J. Grafenstein, D. Cremer, *Chem. Phys. Lett.* **279**, 9 (1997).
13. T. Muller, Y. Zhao, J. B. Lambert, *Organometallics* **17**, 278 (1998).
14. T. Nishinaga, Y. Izukawa, K. Komatsu, *J. Am. Chem. Soc.* **122**, 9312 (2000).
15. A. Sekiguchi, T. Matsuno, M. Ichinohe, *J. Am. Chem. Soc.* **122**, 11250 (2000).
16. C. A. Reed, *Acc. Chem. Res.* **31**, 133 (1998).
17. D. Stasko, C. A. Reed, *J. Am. Chem. Soc.* **124**, 1148 (2002).
18. C. A. Reed *et al.*, *J. Am. Chem. Soc.* **121**, 6314 (1999).
19. X-ray data for $C_{39}H_{55}B_{11}Br_6Si$ at 223(2) K with Mo 0.71073 Å. Monoclinic P2(1)/c, a = 12.771(1), b = 29.227(1), c = 13.601(1) Å, β = 102.152(2)°, Z = 4, θ = 1.39° to 23.26°; 7132 independent reflections [R(int) = 0.0556]; 528 parameters; goodness of fit, 1.012; R ($I > 2\sigma$) 0.0397; wR2, 0.0826; largest diff. peak and hole, 0.598; and −0.486 e.Å^3. Full data have been deposited in the Cambridge Crystallographic Database.
20. J. B. Lambert *et al.*, *J. Organomet. Chem.* **568**, 21 (1998).
21. I. Zharov, B. T. King, Z. Havlas, A. Pardi, J. Michl, *J. Am. Chem. Soc.* **122**, 10253 (2000).
22. R. West *et al.*, *J. Am . Chem. Soc.* **119**, 4972 (1997).
23. J. B. Lambert, Y. Zhao, H. Wu, W. C. Tse, B. Kuhlmann, *J. Am. Chem. Soc.* **121**, 5001 (1999).
24. J. Herzfeld, A. E. Berger *J. Chem. Phys.* **73**, 6021 (1980).

25. Supported by the National Science Foundation CHE 0095206 (to C.A.R.), CHE 0091162 (to J.B.L.), CHE-9982362 and ACS PRF Grant 35320-G6 (to L.J.M.), and Department of Education Graduate Fellowship (GAANN) P200A000208 (to D.W.E.).

2 May 2002; accepted 19 June 2002

Laminar Growth of Ultrathin Metal Films on Metal Oxides: Co on Hydroxylated α-Al_2O_3(0001)

S. A. Chambers,[1]* T. Droubay,[1] D. R. Jennison,[2] T. R. Mattsson[2]

Metals deposited in vacuum on metal oxides such as alumina normally grow as three-dimensional clusters because of weak adatom-substrate interactions. This tendency hinders our ability to form interfaces of ultrathin, laminar metal films on oxides for use in microelectronics and other technologies where nanostructural control is desired. We present experimental and theoretical results showing that room temperature Co deposition on fully hydroxylated clean sapphire (α-Al_2O_3) produces a surface chemical reaction that leads to laminar growth, despite a large mismatch in lattice constants. This process should be applicable to a wide range of metals and metal oxides.

Durable interfaces between disparate materials, such as metals and metal oxides (*1*), are critical for nanotechnology [e.g., for the manufacture of microelectronics (*2*), seals, and sensors]. We lack the ability to form multilayer structures of metals and oxides in which the interface is strong and ultrathin layers grow in a laminar fashion. In contrast, nonlaminar island growth is often seen, because adatom-adatom interactions are stronger than adatom-substrate interactions. In this case, the surface–free energy change for film growth [$(\Delta\gamma) = (\gamma_{film} + \gamma_{int} - \gamma_{sub})$] is greater than zero because the surface free energy of the film (γ_{film}) may be larger than that of the substrate (γ_{sub}), and the interface free energy (γ_{int}) is small because of weak adsorbate-substrate interactions. In addition, metal/metal-oxide interfaces are of critical importance for understanding heterogeneous catalysis (*3*), corrosion, and adhesion.

Co on alumina is especially important because of a proposed use in magnetoresistive random access memory (*2*). A thin (~1 nm) alumina layer is sandwiched between two magnetic layers to form a tunnel junction. High-quality alumina films can be produced by plasma oxidation of Al films (*2*). However, it is problematic to grow a thin magnetic Co layer on top of the alumina film in a laminar fashion with a durable interface.

Ultrathin (<1 nm) alumina films have also been produced by NiAl (*4*) and Ni_3Al (*5*) oxidation. Almost all metals deposited on these oxide films form three-dimensional (3D) islands (*6*). There is no Ostwald ripening at room temperature, and island sizes show a narrow dispersion. Sizes may also be controlled by hydroxylating the surface by depositing Al metal, which in turn dissociates water. Adsorbed hydroxyls apparently serve as nucleation centers (*3*, *7*, *8*), which has been confirmed by first principles theory (*9*). Patches of surface hydroxyl on thin-film alumina are suggested to partially oxidize Rh to Rh^{+1}, accompanied by OH^- reduction to H (*7*, *8*). However, scanning microscope evidence (*8*) suggests that 3D clusters persist, despite the presence of surface OH. The atomic-scale morphology of these surfaces is unknown, and although Al-OH structures have been suggested (*7*, *8*), there could also be OH within or on the oxide surface produced by protons ($H^+ + O^{2-}$), together with surface O vacancies. For a planar interface, it is desirable to start from a smooth, well-defined oxide surface.

A model substrate for such studies is polished α-$Al_2O_3(0001)$ that has not been ion sputtered. The normal termination of ultrahigh vacuum (UHV)–clean α-$Al_2O_3(0001)$ consists of one Al ion for every three O ions. The terminal Al ions are only slightly above the plane of the close-packed O (*10*). However, when clean α-$Al_2O_3(0001)$ is exposed to 1 Torr or more of water, the surface becomes fully terminated by OH (*11*). Thus, samples exposed to ambient conditions have this termination.

In contrast to the situation with a partial (*12*) or mixed OH surface coverage (*7*, *8*), a metal overlayer should interact more weakly with a completely OH-terminated surface than with clean sapphire. The surface ionic charges are then uniform and smaller (1– versus 3+ and 2–), and most transition metals adhere principally by polarization (*13*, *14*), as suggested long ago (*15*).

In the present investigation, we have found that Co deposited in ultrahigh vacuum on fully hydroxylated α-$Al_2O_3(0001)$ reacts to form metal cations within the terminal oxide layer, causing them to bind strongly both to the substrate and to metallic atoms above. These ionic anchors change the morphology of the metal growth. Laminar growth is achieved, because the density of anchors, ~0.1 monolayer (ML), is sufficient to prevent 3D-island formation. Surface diffraction reveals crystalline Co after only a few atomic layers despite an ~7% Co-Co versus O-O spacing mismatch. First principles density functional theory (DFT) predicts that this reaction, involving Co adatoms and made possible only by adjacent surface OH groups, is strongly exothermic:

$$2OH^- + Co^0 \rightarrow 2O^{2-} + H_2 + Co^{2+} \tag{1}$$

As shown below, the barrier for reaction 1 is too high for it to occur thermally; i.e., the adatom could easily diffuse to a nucleation site for 3D growth before reaction 1 occurs. Instead, we show that the heat of adhesion is sufficient to overcome the barrier, even if the atom lands well off the reaction site. Because hydrogen is involved, the time scale for the complete process is only ~0.1 ps, whereas several ps are required for thermalization. In addition, this reaction becomes endothermic if the Co is part of a cluster of four or more Co atoms. The oxidized Co, or Co(II), is the anchor; thus, we suggest that the above reaction is central to the overall process.

All experiments were carried out in a system described in detail elsewhere (*16*). Bulk α-$Al_2O_3(0001)$ crystals were cleaned by acetone and isopropanol sonication, followed by oxygen plasma cleaning in vacuo at room temperature. The resulting surfaces were well ordered, exhibiting a (1 × 1) reflection high-energy electron diffraction (RHEED) pattern, which indicates an atomically flat surface with large terrace widths. These surfaces were free of carbon but retained trace amounts (≤0.04 ML total) of Mg and Ca. These impurities are likely implanted in the near-surface region as a result of the polishing process. In addition, this impurity level amounts to at most ~10% of the Co initially deposited and is thus not expected to affect the outcome of the experiment.

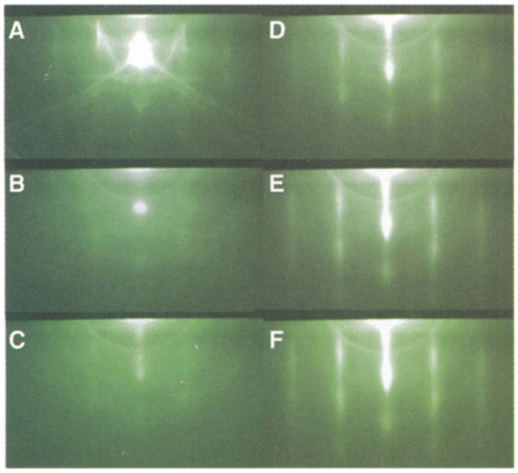

Fig. 1. RHEED patterns in the $(1\bar{1}00)$ zone axis for clean α-$Al_2O_3(0001)$ (**A**), and as a function of coverage for Co deposition with the substrate at ~300 K. (**B**, **C**, **D**, **E**, and **F**) correspond to coverages of 2, 4, 6, 8, and 10 ML, respectively. A quasi-epitaxial structure is achieved, despite the 7% lattice mismatch between Co(0001) and the close-packed O-plane of α-$Al_2O_3(0001)$.

All Co depositions were carried out with the substrate at room temperature. Each deposition is quantified relative to α-$Al_2O_3(0001)$, where 1 ML is equal to 1.58×10^{15} atoms/cm^2, the density of a close-packed O layer. The deposition rate was 0.40 ML per min. All x-ray photoelectron spectroscopy (XPS) measurements were obtained with a SES 200 analyzer (Gammadata Scienta, Uppsala, Sweden) and monochromatic AlKα x-radiation. Spectra were obtained at a 10° take-off angle to enhance surface sensitivity. A low-energy (1 to 2 eV) electron-flood gun was used to neutralize the photoemission charge that accumulated on the insulating sapphire substrate. All binding energies were shifted so that the O 1s peak associated with bulk sapphire fell at 531.0 eV (*17*).

Figure 1 shows a series of RHEED patterns measured in the $(1\bar{1}00)$ zone axis, obtained in real time, during the deposition of Co. After the formation of a highly disordered interfacial layer during the first few MLs, order was gradually restored as the pattern emerged for (0001)-oriented Co. The streak spacing, which is sensitive to the in-plane lattice parameter in the direction perpendicular to the electron beam, increased until ~5 ML, when it became that expected for fully relaxed Co. The appearance of streaks in the RHEED pattern for the fully developed film suggests that the film was quite flat, which is consistent with layer-by-layer growth on the sapphire surface and an absence of 3D islanding. To determine the actual flatness of the multilayer film, we turned to tapping mode AFM images obtained in air after the full 10-ML film had been grown. One such representative image is shown in Fig. 2. There is no appreciable height variation across the film surface, and the widely separated steps, which are normally nucleation sites, are not decorated by 3D islands. Therefore, we had the surprising result that Co fully covered the hydroxylated α-$Al_2O_3(0001)$ surface. This result would not have been expected unless some kind of chemical reaction occurred. XPS provides evidence that such a reaction happened.

---

[1] Pacific Northwest National Laboratory, Post Office Box 999, MSK8–93, Richland, WA 99352, USA. [2] Sandia National Laboratories, Post Office Box 5800, Albuquerque, NM 87185–1415, USA.

*To whom correspondence should be addressed. E-mail: sa.chambers@pnl.gov

O 1s spectra reveal that the α-Al_2O_3(0001) surface, prepared as described above, is terminated with a full ML of hydroxyl. In addition to the lattice O 1s peak at 531.0 eV in Fig. 3A, a second peak is present at 532.7 eV, caused by surface OH, which in turn resulted from polishing in aqueous media and/or exposure to atmospheric humidity. Room temperature oxygen plasma cleaning does not remove the OH layer, in contrast to high temperature vacuum annealing, which is known to partially remove surface OH (*12*). We deduce a 1-ML coverage by interpreting the ratio of OH to lattice oxygen O 1s intensities, using a simple inelastic attenuation model with an electron attenuation length of 20 Å (*18*). This result is consistent with recent work in which crystal truncation rod (CTR) x-ray diffraction was used to investigate α-Al_2O_3(0001) after water washing (*11*). The CTR experiments were carried out at atmospheric pressure with ambient humidity levels. Thus, a layer of physisorbed water was also observed, which is not present in our experiments because of the UHV conditions. Nevertheless, CTR measurements and the associated modeling led to the conclusion that the α-Al_2O_3(0001) surface is entirely terminated by a close-packed OH layer. The 1.7-eV chemical shift between lattice and hydroxyl oxygen is in excellent agreement with earlier work (*19*). Water chemisorbed on oxide surfaces typically results in O 1s peaks shifted 2.5 to 3.0 eV to higher binding energy relative to the lattice oxygen peak (*20*). On sapphire, the shift is less (*12*).

Figure 3B shows a grazing-emission O 1s spectrum after deposition of 0.8 ML Co. A clear reduction in the intensity of the OH-derived feature relative to the oxidic peak is apparent and corresponds to removal of ~0.4 ML of OH. This result suggests that incident Co atoms displace hydrogens in the terminal layer. As this process occurs, there is clear spectral evidence for the oxidation of a fraction of the incident Co to the +2 formal oxidation state. Figure 4 shows Co 2p spectra after deposition of 0.3 ML (A) and 0.8 ML (B) of Co, along with spectra for thin-film polycrystalline Co metal (C), and epitaxial films of CoO (D) and γ-Co_2O_3 (E), both grown on MgO(001) (*21*). The latter three spectra are references for the 0, +2, and +3 formal oxidation states of Co. The dominant peak for both Co coverages on sapphire falls very close to that measured for elemental Co, although the 0.3 ML spectrum is shifted to higher binding energy by 0.5 eV. The latter result is probably due to less efficient final-state screening in this partial ML. As the Co coverage approaches a full ML, the binding energy approaches that for bulk Co metal [778.3 eV (*17*)], whereas multilayer films of Co on α-Al_2O_3(0001) exhibit binding energies of 778.1 to 778.2 eV. In addition, there is Co 2p intensity at the binding energy exhibited for Co(II) for both coverages. The ratio of Co(II) to Co(0) is greater at 0.3 ML than at 0.8 ML, suggesting that the initial Co atoms incident on the surface undergo a redox reaction with surface hydroxyls, resulting in H_2 and Co(II). Unfortunately, the Co $2p_{3/2}$ peak energy is very close to that of the Co $L_2M_{23}M_{45}$ (^1P) Auger feature at the AlKα x-ray energy. This fact complicates the line shape, making it very difficult to quantitatively separate the Co(0) and Co(II) contributions. The Co(0) peak at both coverages is much broader than that measured for Co metal, suggesting inequivalent bonding positions for the unoxidized Co atoms on the surface. As described below, this observation supports conclusions drawn from theoretical predictions of the interface structure.

DFT (*22*, *23*) calculations used the Vienna ab initio simulations package (*24*) in the local density (LDA) (*25*) and PW91 (*26*) generalized gradient approximations (GGA). The study used the ultrasoft pseudopotentials of Vanderbilt (*27*), a plane wave cutoff of 396 eV, and a large *c* axis (with a vacuum gap of ~15 Å) to eliminate long-range electrostatic interactions. To study sub-ML Co, the *a* and *b* primitive cell axes were doubled, making a supercell of five O layers with 12 O ions each. The bottom three O layers and neighboring Al ions were frozen at atom positions appropriate for near-surface layers (*14*). The top surface was relaxed, reactions were studied only on that side, and only a single inverse lattice vector (gamma) was needed. Co required spin-relaxed calculations, but the basic conclusions are independent of magnetism.

Table 1. The LDA(GGA) $2OH^- + Co^0 \rightarrow 2O^{2-} + H_2 + Co^{2+}$ reaction exothermicity (in eV) of isolated spin-polarized ad-clusters, containing from one to four Co atoms, reacting to produce a single molecule of hydrogen from the OH^- terminated sapphire(0001) surface.

Cluster size	ΔE
1 Co	1.7 (1.5)
2 Co	0.47 (0.85)
3 Co	0.13 (0.53)
4 Co	−0.51 (−0.12)

None of the current exchange-correlation functionals is accurate in all situations. A determination of the Pd adhesion energy to an alumina film (*28*) revealed that LDA (GGA) was 15% (40%) low relative to experiment (*29*). We recently traced this problem to surface self-energy errors (*30*), especially important when binding is weak. Our system has all types of binding, with metal/metal-oxide adhesion better given by LDA (*28*, *29*), metal cohesion and covalent bonds better described by GGA (*31*), and polarization near the interface about the same by both methods (*30*).

Because neither method is perfect, we

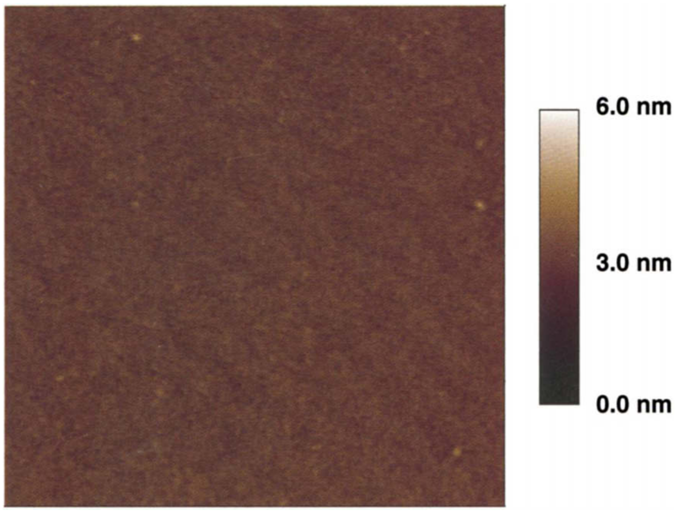

Fig. 2. Tapping-mode AFM image obtained after deposition of 10 ML of Co on α-Al_2O_3(0001) at 300 K. The lateral dimensions are 1 × 1 μm.

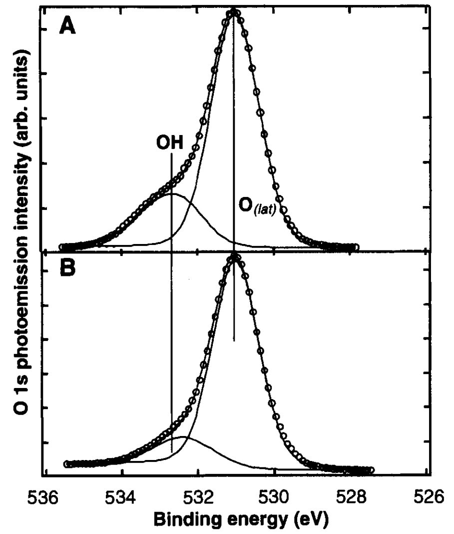

Fig. 3. O 1s core-level spectrum measured at a 10° take-off angle for α-Al_2O_3(0001) after oxygen plasma cleaning (**A**), and the same after ~0.8 ML Co deposition (**B**).

present both LDA and GGA results for the reaction $2OH^- + Co^0 \rightarrow Co^{2+}2O^{2-} + H_2$ in isolated ad-clusters of $n = 1$ to 4 Co atoms. Our principal conclusion is independent of the method. We discard reactions that produce water (*32*).

The highest exothermicity, 1.5 to 1.7 eV, involves a single ad-atom of Co^0 and a final-state with H_2 and Co^{2+} (Fig. 5). The Co^{2+} prefers a surface hollow site adjacent to the two final-state O^{2-} ions. Table 1 summarizes other energy results, showing monotonically decreasing exothermicity with increasing cluster size. When $n = 4$, endothermicity occurs because of a competition between the reaction and metal-metal binding.

A monolayer of free-standing Co shows a tendency to buckle, which is also suggested by the atomic positions in our $n = 3$ and $n = 4$ clusters. Thus, the initial covering is more like a bilayer of metal. However, the uncertainty of film geometry due to the pronounced lattice mismatch precludes computations on the full structure or its adhesion to the substrate.

We now consider kinetic factors. If reaction 1 were thermally driven, the frequency would be given by the temperature; the prefactor, α; and the reaction barrier, E_r. We calculated E_r using the nudged elastic band technique (NEB). NEB (*33*) relies on knowing initial and final states that are connected by a chain of intermediate states to represent the reaction path. GGA results are shown in Fig. 5B. A single Co atom starts at the preferred on-top O-site, translates to the reaction site near the O-bridge and then to the final-state hollow site. With typical prefactors ($\alpha = 10^{12}$ to 10^{13}), the thermal time scale for the reaction, given by $\alpha\exp(E_r/kT)$, is $\sim 10^{-2}$ to 10^{-3} s. However, the barrier for diffusion is <0.2 eV, because the adsorption energy is ~1.2 eV (*34*), producing diffusive hops, each ~1 to 10 ns. Clearly, a thermal process cannot explain our observation of a dispersed 0.1 ML of Co(II).

"Hot" surface reactions occur using the heat of adsorption to overcome a barrier (*35*, *36*). Here, the kinetic energy of an arriving Co atom is 1.25 to 1.35 eV (*34*), indicating a velocity of ~20 Å/ps. The equilibrium height at the O-O bridge is only 0.22 Å above the transition-state site, and the lateral distance from the on-top O position (Fig. 5A) is ~1.4 Å. Therefore, after arrival, it takes less than 0.1 ps for Co to impact the two O ions and promote H_2 formation by weakening the two O-H bonds. This process is more than an order of magnitude faster than thermalization times. In addition, reactions and fluctuations (*37*) involving hydrogen occur on an ~0.1 ps time scale, whereas heavier atoms need many ps. Thus, we propose that Co(II) anchors are generated directly upon impact, and those atoms that substantially miss the bridge sites (e.g., hit or slide into the hollow sites) do not undergo reaction and remain metallic, as observed. Co(II) ions locally pin these Co atoms. (A single metallic Co atom binds by ~1.2 eV to the Co ion.) Theory explains the observation that, with more Co added (0.8 ML), no additional Co(II) is made (Fig. 4). Table 1 shows that the reaction stops if $n > 3$, which is achieved for >0.3 ML. Thus, the surface retains much OH, as observed (Fig. 3).

In summary, we found that a fully hydroxylated sapphire surface promotes laminar growth in a Co overlayer, resulting in a planar interface only a few atomic layers thick. The surface is easily formed by exposing sapphire to >1 Torr of water and then removing impurities by oxygen plasma cleaning, which does not remove surface OH. Because the redox process is likely caused by a hot reaction, it should also occur at a low temperature. Film stability should also be probed at higher temperatures. The only requirements for this process to occur are adjacent surface OH and a metal atom kinetic energy that can overcome the relevant reaction barrier.

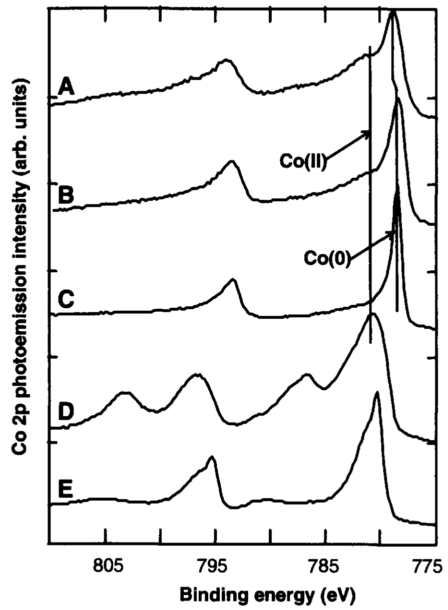

Fig. 4. Co 2p core-level spectra at a 10° take-off angle for 0.3 ML (**A**) and 0.8 ML (**B**) on α-Al_2O_3 (0001). Also shown are normal-emission spectra for reference surfaces of thin-film Co/Si(001) (**C**), CoO/MgO(001) (**D**), and γ-Co_2O_3/MgO001) (**E**). Comparison with the reference spectra reveals that the Co ad-layer contains a mixture of Co(0) and Co(II).

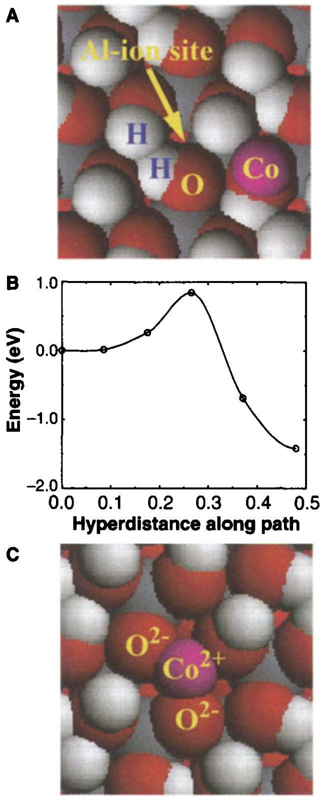

Fig. 5. The preferred initial-state geometry for the OH terminated surface in the presence of isolated Co atoms (**A**). Note the Al-site hollow (yellow arrow). (Pink is Co, red is O, white is H, and gray is Al.) The computed activation barrier for reaction 1 (**B**). Here, the zero is set at the initial-state energy. The barrier height is ~0.85 eV by GGA, occurring when the Co atom is near the O-O bridge site. The reaction final-state geometry for the Co adatom (**C**).

References and Notes

1. G. Thornton, *Faraday Discuss. Chem. Soc.* **114**, (2000).
2. S. Tehrani *et al.*, *IEEE Trans. Magn.* **36**, 2752 (2000).
3. G. Ertl, H.-J. Freund, *Phys. Today* **52**, 32 (1999).
4. R. M. Jaeger *et al.*, *Surf. Sci.* **259**, 235 (1991).
5. A. Rosenhahn, J. Schneider, C. Becker, K. Wandelt, *Appl. Surf. Sci.* **142**, 169 (1999).
6. M. Bäumer, H.-J. Freund, *Prog. Surf. Sci.* **61**, 127 (1999).
7. J. Libuda *et al. Surf. Sci.* **384**, 106 (1997).
8. M. Heemeier *et al.*, *Catal. Lett.* **68**, 19 (2000).
9. A. Bogicevic, D. R. Jennison, *Surf. Sci. Lett.* **437**, L741 (1999).
10. P. Guenard, G. Renaud, A. Barbier, M. GautierSoyer, *Surf. Rev. Lett.* **5**, 321 (1998).
11. P. J. Eng *et al.*, *Science* **288**, 1029 (2000).
12. C. Niu *et al.*, *Surf. Sci.* **465**, 163 (2000).
13. A. Bogicevic, D. R. Jennison, *Phys. Rev. Lett.* **82**, 4050 (1999).
14. C. Verdozzi, D. R. Jennison, P. A. Schultz, M. P. Sears, *Phys. Rev. Lett.* **82**, 799 (1999).
15. A. M. Stoneham, *Appl. Surf. Sci.* **14**, 249 (1983).
16. S. A. Chambers, *Surf. Sci. Rep.* **39**, 105 (2000).
17. J. F. Moulder, W. F. Stickle, P. E. Sobol, K. D. Bomben, *Handbook of X-ray Photoelectron Spectroscopy* (Perkin-Elmer, Eden Prairie, MN, 1992).
18. S. Tanuma, C. J. Powell, D. R. Penn, *Surf. Int. Anal.* **11**, 577 (1988).
19. J. L. Hunta-Rosso, M. F. Hochella Jr., *Geochim. Coscochim. Acta* **60**, 305 (1996).
20. T. Kendelewicz *et al.*, *Surf. Sci.* **453**, 32 (2000).
21. S. A. Chambers *et al.*, *J. Mag. Mag. Mat.* **246**, 124 (2002)
22. P. Hohenberg, W. Kohn, *Phys. Rev.* **136**, B864 (1964)
23. W. Kohn, L. J. Sham, *Phys. Rev.* **140**, A1133 (1965).
24. The Vienna ab initio simulations package was developed at the Institut für Theoretische Physik of the Technische Universität Wien, as described in G. Kresse, J. Hafner, *Phys. Rev. B* **54**, 11169 (1996).
25. J. Perdew, A. Zunger, *Phys. Rev. B* **23**, 5048 (1981).
26. J. P. Perdew *et al.*, *Phys. Rev. B* **46**, 6671 (1992).
27. D. Vanderbilt, *Phys. Rev. B* **41**, 7892 (1990).
28. K. H. Hansen, *et al.*, *Phys. Rev. Lett*, **83**, 4120 (1999).

29. D. R. Jennison, A. Bogicevic, *Surf. Sci. Lett.* **464**, 108 (2000).
30. A. E. Mattsson, D. R. Jennison, in preparation.
31. L. A. Curtiss, K. Raghavachari, G. W. Trucks, J. A. Pople, *J. Chem. Phys.* **94**, 7221 (1991).
32. The endothermic reaction $2OH^- + Co^0 \rightarrow O^{2-}Co^0 + H_2O$ does not produce Co(II).
33. G. Mills, H. Jonsson, G. K. Schenter, *Surf. Sci.* **324**, 305 (1995).
34. The LDA binding energy (1.08 eV) is likely below the real value (*28*). Estimating the surface self-energy correction (*30*) produces this estimate. In addition, the thermal energy of the source contributes 0.11 eV.
35. J. Strömquist *et al.*, *Surface Science*, **397**, 382 (1998).
36. M. Persson *et al.*, *J. Chem. Phys.* **110**, 2240 (1999).
37. K. C. Hass, W. F. Schneider, A. Curioni, W. Andreoni, *J. Phys. Chem. B* **104**, 5527 (2000).

38. We thank R. R. Stumpf for critical comments and J. Strömquist for useful discussions. Pacific Northwest National Laboratory (PNNL) and Sandia National Laboratory (SNL) are multiprogram laboratories operated for the U.S. Department of Energy by Battelle Memorial Institute under Contract DE-AC06-76RLO 1830 (PNNL), and by Sandia Corporation, a Lockheed Martin Company, under Contract DE-AC04-94AL85000 (SNL). The experimental work was conducted in the Environmental Molecular Sciences Laboratory, a national scientific user facility sponsored by the Department of Energy's Office of Biological and Environmental Research and located at PNNL. T.R.M. acknowledges the Motorola/SNL computational materials Cooperative Research and Development Agreement. S.A.C. and T.D. were supported by the U.S. Department of Energy, Office of Science, Office of Basic Energy Sciences, Division of Materials Science at PNNL.

30 April 2002; accepted 14 June 2002

Detection of a Large-Scale Mass Redistribution in the Terrestrial System Since 1998

Christopher M. Cox[1]* and Benjamin F. Chao[2]

Earth's dynamic oblateness (J_2) had been undergoing a decrease, according to space geodetic observations over the past 25 years, until around 1998, when it switched quite suddenly to an increasing trend that has continued to the present. The secular decrease in J_2 resulted primarily from the postglacial rebound in the mantle. The present increase, whose geophysical cause(s) are uncertain, thus signifies a large change in global mass distribution with a J_2 effect that considerably overshadows that of mantle rebound.

Earth's mean tide-free dynamic oblateness $(J_2) \equiv [C - (A + B)/2]/MR^2 = 1.082627 \times 10^{-3}$, where $C > B \geq A$ are Earth's mean principal moments of inertia and M and R are the mean mass and radius, respectively. Satellite laser ranging (SLR) has yielded precise determination of the temporal variation in the low-degree spherical harmonic components of Earth's gravity field, beginning with the initial observations of J_2 change made by observing Lagoes-1 satellite orbital node accelerations (*1*, *2*). More recent studies have extended the knowledge to higher degree zonals and examined the annual signals in the low-degree geopotential (*3–5*). The estimated values of the J_2 rate have ranged from -2.5×10^{-11} year^{-1} to -3×10^{-11} year^{-1}.

The extension of comprehensive solutions for low-degree geopotential zonal, static, annual, and rate terms and the 9.3- and 18.6-year ocean tide amplitudes to include data since 1997 has resulted in increasingly significant changes in the estimated J_2 rate and 18.6-year tide amplitude (*4*). These changes implied that the models for these terms were not accommodating the observed signal. Consequently, we estimated a time series of low-degree (maximum degree of 4) static geopotential solutions using SLR observations of 10 satellites over the period from 1979 to 2002. The inclusion of multiple orbital inclinations improves separation of the higher degree zonal components and allows recovery of the gravity coefficients over shorter time periods. All processing used the same algorithms used to develop the EGM96S satellite–only gravity model and to calibrate that model's covariance (*5*). The 18.6-year and much smaller 9.3-year tide amplitudes were set to the values estimated in the comprehensive solution with data from 1979 through 1997 (*4*). The applied 18.6-year tide amplitude of 1.41 cm has the equivalent J_2 amplitude of 1.67×10^{-10}. The 18.6-year tide–J_2 effect is minimized (that is, the geopotential is less oblate) when the lunar node is 0 degrees, which occurred in mid-October 1987.

Shown in Fig. 1 is the estimated J_2 as a function of time, $J_2(t)$. Lageos-1 data are present throughout, and Starlette data are present from January 1980 onward. Data completeness issues precluded the use of the earlier Starlette and Lageos-1 data. Other satellites were added when launched: Ajisai from August 1986 and Lageos-2 and several other satellites from 1992 onward. TOPEX/POSEIDON (T/P), which is also tracked by the Détermination d'Orbite et Radiopositionnement Intégrés par Satellite system, was added in January 1993. The formal uncertainties shown reflect the SLR data weights derived from the calibration of the comprehensive 19-year solution and should be realistic (*6*).

Dominant in $J_2(t)$ is a seasonal signal of amplitude 3.2×10^{-10}, which is driven by meteorologic mass redistribution in the atmosphere-hydrosphere-cryosphere system (*7–10*). Also plotted in Fig. 1 is the atmospheric contribution calculated according to the National Center for Environmental Prediction (NCEP) reanalysis data (*11*), including the inverted-barometer (IB) correction (*12*). Subtraction of this signal and further empirical removal of the residual seasonal signals (which are attributable to the poorly known seasonal mass redistribution in the oceans and land hydrology) result in a nonatmospheric and nonseasonal $J_2(t)$ (Fig. 2).

A linear fit to the observed J_2 through 1996 shows a decrease in J_2 of -2.8×10^{-11} year^{-1} (Fig. 2). For this period, the uncertainty for the J_2 rate in the comprehensive solution (which considers the correlation with the 18.6-year tide) is 0.4×10^{-11} year^{-1}. Despite the lack of data before 1979, the results are in excellent agreement with estimates of the J_2 rate that included those data (*2*). The secular drift results primarily from postglacial rebound (PGR) (*2*, *13*, *14*) in the mantle, plus various secondary contributions of climatic and anthropogenic origin (for example, reservoirs, which are an order of magnitude too small to explain the recent observations) (*4*, *15*, *16*). At some time during 1997 or 1998, the trend reversed. The post-1996 points have deviated from the pre-1997 slope by about six times the uncertainties, on average, over that period. A linear fit from 1997 onward yields a rate of $+2.2 \times 10^{-11}$ year^{-1}. On the basis of the comprehensive solutions, the uncertainty for this rate is $\sim 0.7 \times 10^{-11}$ year^{-1}; however, because of the nonlinearity in $J_2(t)$, the slope can vary by more than the uncertainty value, depending on the period fitted. Another departure may exist around 1980, but excepting a few data points the deviation is only one to two times the uncertainties, making the importance unclear.

An increase in J_2 means a net transport of mass from high to low latitude (the nodal lines of J_2 are ± 35.3° latitude). Transport of terrestrial water and/or ice mass to the oceans is one likely cause, because most of the ice mass resides in high-latitude polar caps and glaciers. As an example of the mass flux involved, imagine one fictitious scenario that

---

[1] Raytheon Information Technology and Scientific Services (ITSS), [2] Space Geodesy Branch, NASA Goddard Space Flight Center, Code 926, Greenbelt, MD 20771, USA.

*To whom correspondence should be addressed. E-mail: ccox@stokes.gsfc.nasa.gov